From Highly Monodisperse Indium and Indium Tin Colloidal Nanocrystals to Self-Assembled Indium Tin Oxide Nanoelectrodes

Maksym Yarema,[†] Stefan Pichler,[†] Dominik Kriegner,[†] Julian Stangl,[†] Olesya Yarema,[†] Raimund Kirchschlager,[†] Sajjad Tollabimazraehno,[‡] Markus Humer,[†] Daniel Häringer,[§] Manfred Kohl,[§] Gang Chen,[†,*] and Wolfgang Heiss[†,*]

[†]Institute of Semiconductor and Solid State Physics, and [‡]Center for Surface and Nanoanalytics, University Linz, Linz, Austria and [§]Institute of Microstructure Technology, Karlsruhe Institute of Technology, Germany

Optically transparent indium tin oxide (ITO) electrodes are widely used as components of optoelectronic devices, including liquid crystal displays, solution processed light emitting diodes, solar cells, and photodetectors.[1−3] Whereas industrial ITO films are predominantly prepared by deposition from vapor phase, the worldwide shortcoming of indium resources triggered a search for novel, material-effective methods for preparation of patterned ITO electrodes, including also deposition from nanoparticle solutions.[4−7] Since electrodes from ITO nanoparticle inks usually suffer from low conductivity, improvements are required, which are suggested to be obtainable by optimizing particle size distributions and composition homogeneities.[7] While such efforts are reported for ITO nanoparticle inks,[4−7] in this work we show an alternative procedure toward a material effective fabrication of nanopatterned ITO electrodes, based on (i) the synthesis of monodisperse indium and indium tin ($In_{1−x}Sn_x$) colloidal nanocrystals (NCs) with desired size and composition, (ii) the preparation of nanosized patterns from $In_{1−x}Sn_x$ NCs on structured substrates, and (iii), oxidation of the NC patterns to convert the $In_{1−x}Sn_x$ NCs to compact, conductive, and transparent ITO electrodes.

Due to the lack of appropriate synthesis recipes for colloidal $In_{1−x}Sn_x$ NCs in the literature, we introduce here a novel synthetic method. It is based on the hot-injection of mixtures of indium and tin silylamide salts into a coordinating solvent. The nucleation rate and thus the final size of

ABSTRACT
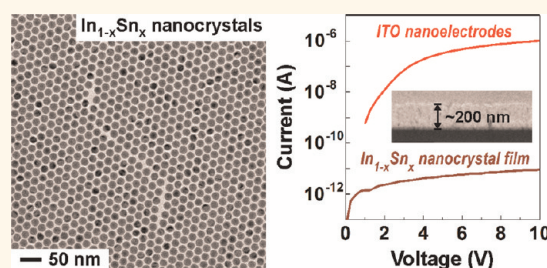
Indium tin oxide (ITO) nanopatterned electrodes are prepared from colloidal solutions as a material saving alternative to the industrial vapor phase deposition and top down processing. For that purpose highly monodisperse $In_{1−x}Sn_x$ ($x < 0.1$) colloidal nanocrystals (NCs) are synthesized with accurate size and composition control. The outstanding monodispersity of the NCs is evidenced by their self-assembly properties into highly ordered superlattices. Deposition on structured substrates and subsequent treatment in oxygen plasma converts the NC assemblies into transparent electrode patterns with feature sizes down to the diameter of single NCs. The conductivity in these ITO electrodes competes with the best values reported for electrodes from ITO nanoparticle inks.

the NCs are controlled by a second injection, containing small amounts of strongly reducing superhydride. Adding lithium-silylamide results in extremely monodisperse NC batches, exhibiting a strong tendency to form ordered superstructures upon slow destabilization or solvent evaporation. These pronounced self-assembly properties of indium and $In_{1−x}Sn_x$ NCs makes the 3-step approach toward ITO electrodes, demonstrated in this paper, advantageous in respect to the preparation of electrodes directly from ITO-nanoparticle solutions
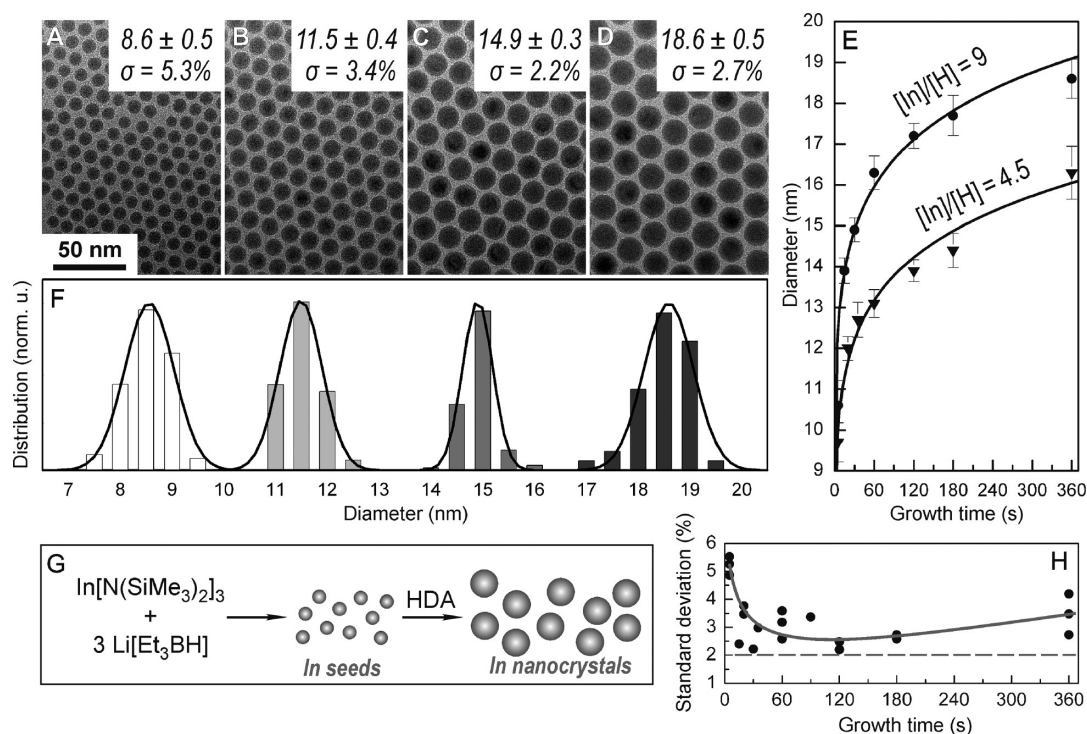
Figure 1. (A–D) Transmission electron microscopy images of indium NCs with different sizes. (E) Size of indium NCs as a function of growth time ([In]/[H] is the molar ratio between $In[N(SiMe_3)_2]_3$ and $Li[Et_3BH]$). (F) Size distributions of the four different batches of indium NCs shown in panels A–D. (G) Proposed mechanism of indium NC formation. (H) Standard size deviations of the indium NC size distributions as function of growth time.

or inks, which suffer usually from size, shape, and composition inhomogeneity.[4−7] On one hand, ordering leads to a minimum of voids between the NCs, and high space filling factors can be obtained in simple drop casted films, which should finally improve the film conductivity. On the other hand, the narrow size dispersion allows also the fabrication of nanosized electrodes with dimensions down to the size of a single NC, as is demonstrated to be feasible by making use of the "damascene" process.[8]

The oxidation of the NCs in this work is performed by an oxygen plasma, which does not only convert the $In_{1−x}Sn_x$ NC films into ITO electrodes, but also allows interesting insights into the oxidation process itself. The oxidation results in an increase of NC diameter, partly due to an increase of the lattice parameter, but mostly due to the formation of hollow cavities in the NCs centers, caused by the nanoscale Kirkendall effect.[9] While the plasma treatment also causes the NC assemblies to become transparent over the whole spectral region, the conductivity is optimized by a further moderate heat treatment performed in air, as is also a standard for electrodes prepared from ITO nanoparticles.[4,6,7] The conductivity, measured in homogeneous thin films obtained by our method, is at least equal to the best values reported so far for electrodes prepared from ITO nanoparticle inks.[4−7] These properties make our ITO electrodes promising for future application and especially it enables, for

example, the development of all-nanoparticle solution-processed optoelectronic devices.

RESULTS AND DISCUSSION

High Precision Synthesis of $In_{1−x}Sn_x$ Colloidal Nanocrystals. The starting point for the preparation of ITO nanopatterned electrodes from solutions is the synthesis of $In_{1−x}Sn_x$ colloidal NCs. To obtain good film forming properties and finally high conductivity, our focus is here to obtain monodisperse NCs with controlled size and accurately regulated composition. Since commercial ITO films contain typically 90% of In_2O_3 and 10% of SnO_2 it is sufficient to tune the Sn concentrations x from 0 up to 10%, to finally obtain optimized performance of the electrodes. From the few reports about $In_{1−x}Sn_x$ nanoparticles,[10,11] none of these are within the desired composition range. Pure indium NCs have been obtained by few different synthetic routes,[12−16] but also in these cases either size control or high monodispersity could not be demonstrated, which is in contrast to our approach, providing a high precision in the control of both of these parameters (Figure 1A–F). This synthesis we demonstrate first for pure indium NCs. Our method is based on two subsequent injections into a coordinating solvent, hexadecylamine (HDA), kept at a temperature of 200 °C. The first injection contains a mixture of indium(III) tris[bis(trimethylsilyl)amide], $In[N(SiMe_3)_2]_3$, and lithium bis(trimethylsilyl)amide, $Li[N(SiMe_3)_2]$, solved in toluene.
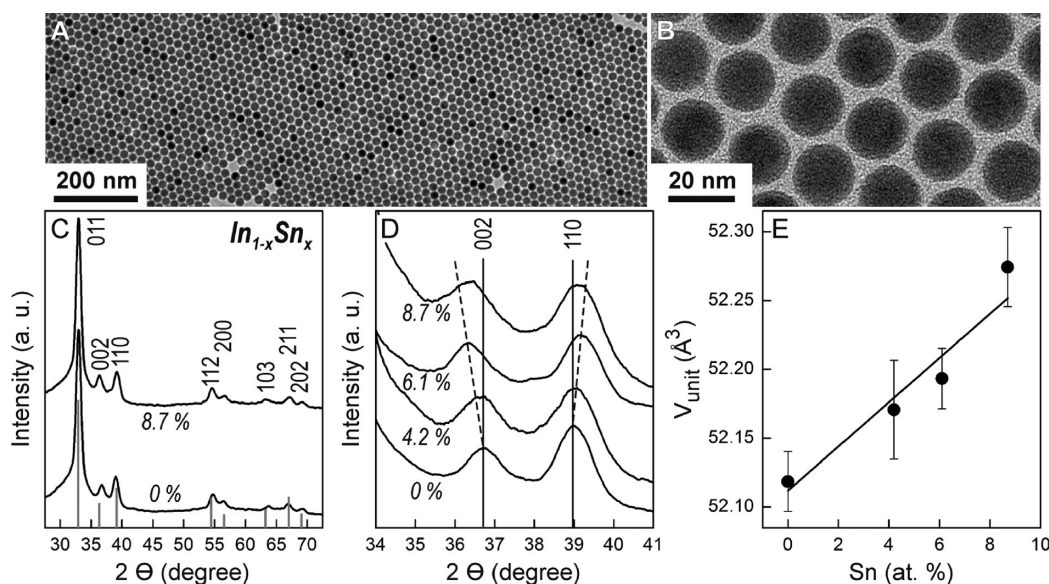
Figure 2. (A,B) Transmission electron microscopy images of $In_{1-x}Sn_x$ NCs with $x = 6.1\%$. (C) Two wide-angle X-ray diffraction (XRD) spectra of $In_{1-x}Sn_x$ NCs, with $x = 0\%$ and $x = 8.7\%$. (D) Specific angle regions of diffraction peaks showing significant shifts with increasing x. (E) Unit cell volume of $In_{1-x}Sn_x$ NCs, extracted from fits of wide angle XRD spectra.

We found no thermal decomposition of $In[N(SiMe_3)_2]_3$ in HDA up to at least 10 min. Thus, with a second injection a solution of lithium triethylborohydride, $Li[Et_3BH]$, a strong reducing agent known also as superhydride,[17] is added. The superhydride reduces the trivalent indium from $In[N(SiMe_3)_2]_3$ to its neutral metallic form, and thus it initiates the nuclei formation. Since $In[N(SiMe_3)_2]_3/Li[Et_3BH]$ molar ratios (abbreviated [In]/[H] in the following) between 10 and 5 are used, after the nucleation step still the majority of $In[N(SiMe_3)_2]_3$ remains, and it is available to gradually decompose on the surface of the indium seeds. The growth after the nucleation proceeds with much slower rate, since it is caused by the moderate reductive properties of HDA.[18] The addition of $Li[N(SiMe_3)_2]$ was found to be essential to obtain narrow size dispersions (Supporting Information, Figure S1), most likely because the $N(SiMe_3)_2$-groups coordinate the surface atoms during the NC growth, as we observed also in the synthesis of monodisperse bismuth NCs.[18]

The nucleation controlled synthesis of indium NCs, described above and sketched in Figure 1G, provides two convenient tools to tune the NC size. Rough adjustments of NC size are obtained by the amounts of $In[N(SiMe_3)_2]_3$ and $Li[Et_3BH]$. Decreasing [In]/[H] results in a decrease of NC size in both cases, by increase of $Li[Et_3BH]$ content because the number of nuclei increases (Figure 1E), or by reducing the $In[N(SiMe_3)_2]_3$, because the amount of remaining indium precursor available for NC growth is reduced (Supporting Information, Figure S2). The second tool to fine-tune the NC size is growth time. Varying the growth time between 7 s and 6 min allows control of the size between 9.7 and 16 nm for [In]/[H] = 4.5 and between 10.5 and 18.3 nm for [In]/[H] = 9 (Figures 1E). The

precision of this size control is better than $^1/_5$ nm, evidenced by the distances between the individual data points in Figure 1E. Furthermore, within this time scale the increase of size dispersion due to Ostwald ripening is negligible, since for all times size dispersions below 6% are achieved and for growth times between 2 and 3 min even values below 3% are obtained (Figure 1F,H). It should also be noted that the indium NCs exhibit almost perfect spherical shape and excellent shape uniformity. This shape might result from the chosen nucleation temperature (155 °C) which is a few degrees above the melting point of bulk indium. Thus, it can be assumed that indium nanoparticles are in liquid form during their nucleation and growth, such that the perfect spherical shape is achieved by minimization of surface energy and their crystallization takes place during the cooling of the colloidal solution.

The synthesis of indium NCs can be easily expanded to $In_{1-x}Sn_x$ by adding certain amounts of commercially available tin(II) bis[bis(trimethylsilyl)amide], $Sn[N(SiMe_3)_2]_2$, to the first injection solution. The alloyed $In_{1-x}Sn_x$ NCs exhibit the same outstanding size uniformity and spherical shape as the bare indium NCs described above (Figure 2A,B). Here the molar Sn/In ratio in the precursor solution is used to adjust the Sn concentration in the NCs. The latter is by a factor of 5 times smaller than the Sn/In ratio in the precursor solution (Supporting Information, Figure S3A), reflecting smaller reactivity of the tin precursor in HDA as compared to that of the indium precursor. The obtained Sn content we found to be independent of growth time (Figure S3B), indicating that the $In_{1-x}Sn_x$ is formed by a continuous coprecipitation of both precursors during the whole reaction time. This fact allows

the independent tuning of Sn content (by Sn precursor concentration) and NC size (by superhydride concentration and growth time) resulting in a high precision control of the In/Sn composition, performed here with up to 10% of Sn content.

Because of the close atomic numbers of indium (49) and tin (50), determining the Sn concentration in the $In_{1-x}Sn_x$ NCs requires some caution. In a first attempt these values are extracted from analysis of energy dispersive X-ray spectra (EDX, Supporting Information, Figure S4). The EDX analysis included measurement of spectra for pure indium and tin NCs, as well as of a bulk indium tin alloy with $x = 10.0\%$. These three reference spectra were used to simulate EDX spectra with various x, which are interpolated to obtain x of the alloyed NCs. These values have been cross checked by wide-angle X-ray diffraction (XRD) experiments (Figure 2C,D). Bulk $In_{1-x}Sn_x$ exhibits the indium crystal structure ($I4/mmm$, $a = 3.253$, $c = 4.943$ Å) up to $x = 13\%$.[19−21] With increasing x, the volume of the unit cell increases, primarily caused by an almost linear elongation of the c-axis. Such an increase of the unit cell volume (Figure 2E) and c-lattice parameter we observe also for the indium tin NCs by the shift of the (002) (Figure 2D) and (103) diffraction peaks toward smaller angles (Figure S5). The (110) diffraction peaks move to higher angles indicating a slight increase of the a-lattice parameter. To evaluate these subtle changes of the lattice parameters, the Pawley method was used to fit the unit cell structure under a symmetry constraint to the measured data. For the NCs the same trends in the x dependence of unit cell volume and lattice parameters are observed as for bulk.[19−21] However, already for pure indium NCs the unit cell volume is found to be decreased by 0.4% in comparison to bulk indium. This deviation is mainly driven by a decrease in the c-lattice parameter, whereas a is found to be increased.

Self-Assembly and Nanocrystal Nanopatterns. To obtain high conductivity in NC assemblies, not only the appropriate choice of material and manipulation of ligand shell but also the quality of assembly matters. Obviously any kinds of voids in the assembly have to be avoided to enable homogeneous current flow through the films. Considering spherical NCs as hard spheres of uniform size, in any type of assembly the minimal void space is given in closely packed sphere arrangements, characterized by a space filling factor of 0.74.[22,23] Typical arrangements of closed packed spheres are given when they are ordered, forming either hexagonal closed packed (*hcp*) or face centered cubic (*fcc*) lattices. Thus, optimizing the ordering in NC films is a required precondition to obtain improved transport properties.

To obtain a first impression on how appropriate the NCs are for self-assembly, their 3-dimensional ordered superstructures are briefly discussed. They are formed by adapting the slow destabilization approach,[24] after
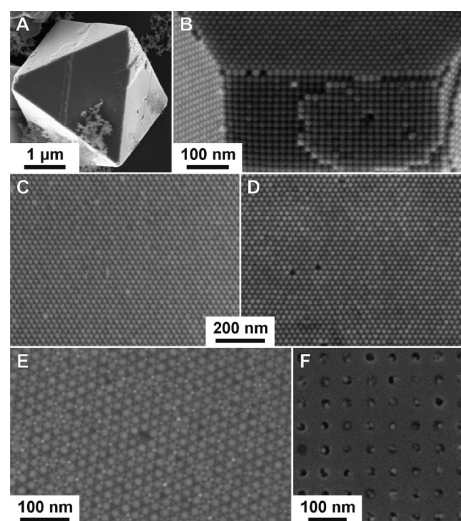

Figure 3. (A) SEM image of a typical self-assembled indium nanocrystal 3D superlattice (supercrystal). (B) View on a {100} plane of the supercrystal and on {111} oriented side facets. (C) Self-assembled surface of the nanocrystal supercrystal. (D) Self-assembled top layer of an indium NC film, deposited on a silicon substrate by drop casting. (E) Binary indium/gold NC superlattice with AlB_2 crystal structure. (F) Individual $In_{0.9}Sn_{0.1}$ NCs deposited into pits, etched into a silicon substrate.

a growth time between 1 and 2 weeks. The superstructures are indeed well-faceted crystallites with sizes of a few micrometers (Figure 3A), thus they contain more than 1×10^7 NCs. Owing to the metallic character of the NCs, scanning electron microscopy (SEM) allows a convenient inspection of the microcrystals surface with sufficient magnification to observe individual NCs and their arrangements (Figures 3B and Supporting Information, Figure S6). This enables a facile determination of the facet orientations and subsequently of the crystal structure. The indium NCs arrange in the *fcc* crystal structure, which also causes the octahedral shape of the microcrystals (Figure 3A and Figure S6). The SEM image in Figure 3C, showing a view on the {111} facet of an indium NC microcrystallite, highlights the perfectness of the self-assembled structure. In this image about 1300 NCs are shown, and the hexagonally ordered arrangement exhibits not even a single void. Actually also a quantitative analysis of the autocorrelation function (ACF) of this image (Figure S7),[25] providing a normalized long-range order parameter of $\xi_{LR} = 0.97$ ($\xi_{LR} = 1$ for a perfect ordered lattice), confirms the outstanding quality of this NC arrangement. Most importantly, however, these results demonstrate the high tendency of the indium NCs to form self-assembled superstructures, a property which is of relevance also for the preparation of thin films. In fact, self-assembled films obtained simply by drop casting indium NCs on silicon substrates exhibit a similar perfect ordering on their surface as that of the 3D crystallites (Figure 3D). The hexagonally closed packed NC superlattice on the NC films surface

provides a normalized long-range ordering parameter of $\xi_{LR} = 0.86$, corresponding to less than 1% of slightly shifted NCs in a model.[25] The appearance of this close to perfect long-range ordering in NC self-assembled films suggest that also for this case space filling factors are achieved, which closely approach the highest possible value of 0.74. Higher space filling factors can only be achieved in special binary superlattices of two differently sized NCs, with well-selected size ratios between the two NC species.[22,26,27] In this case the smaller NCs can for instance fill the voids formed around each big NC, and by this increase the space filling factor. Generally, such binary NC superlattices can also be obtained with our indium NCs, for example, when they are combined with smaller gold NCs. Figure 3E shows a binary In/Au NC superlattice with AlB_2 crystal structure having a space filling factor superior to that of single component close packing.[22] Since such highly ordered binary superlattices are restricted to rather small domain sizes, in the following we concentrate on single component NC assemblies as starting point for electrode fabrication.

The tendency to form highly ordered superstructures and thus 2-dimensional films with high filling factor is a result of the extremely high monodispersity of the indium tin NCs. This uniformity is also beneficial for the preparation of NC nanopatterns, representing intermediate stages toward the formation of ITO nanoelectrodes. The nanopatterns are fabricated by drop casting of the colloidal solution on structured silicon substrates. To achieve real nanopatterns, e-beam lithography was employed for writing the structures into a polymethylmethacrylate (PMMA) e-beam resist. The structures were transferred into the silicon substrates by reactive ion etching. For demonstration, circular pits were fabricated with diameters down to 25 nm. After deposition of a single colloidal droplet onto the nanostructured area and solvent evaporation, NCs cover the whole nanopattern. By wiping off the NCs with a standard polishing cloth, all the NCs from the flat parts in between the pits are removed whereas the pits remain filled by NCs. This method,[8] which is reminiscent to the "damascene" process applied in semiconductor technology for the fabrication of copper conducting paths in silicon based devices, is scaled down here to patterns of NC assemblies containing between approximately 80 NCs (100 nm pit size, Supporting Information, Figure S8) and exactly one $In_{0.9}Sn_{0.1}$ NC (25 nm pit size, Figure 3F). It should be noted also, that the damascene process performed with NCs, where microliter droplets of colloidal solutions are deposited exactly on patterned target areas of the samples, is more material effective than the traditional damascene processes based on vapor phase deposition of metals, covering at least the areas of the whole samples.
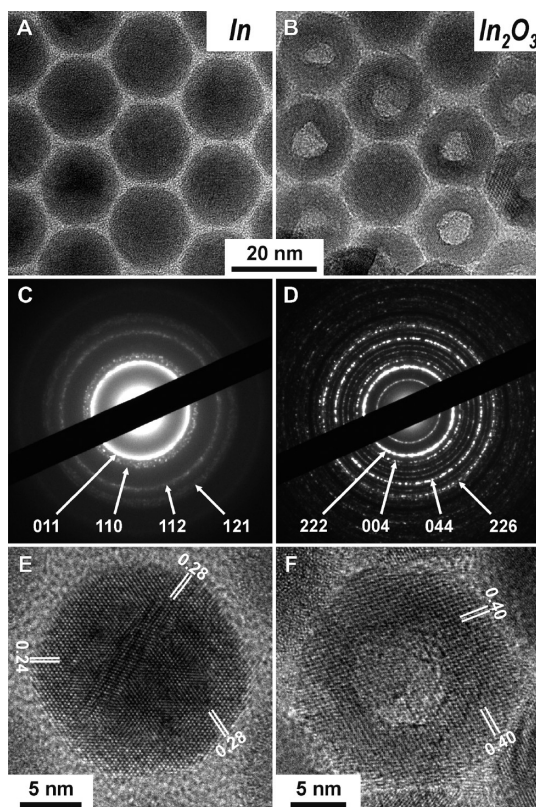

Figure 4. Transmission electron microscopy image (A), selected area electron diffraction (C), and high resolution transmission electron microscopy image (E) of indium and (B,D,F) indium oxide NCs. The indium NC in panel E is viewed in the (111) direction; the indium oxide NC in panel F is viewed in the (100) direction.

Conversion to Indium Tin Oxide (ITO) Electrodes. To convert the $In_{1-x}Sn_x$ NC assemblies into ITO electrodes, an oxidation step is required. The oxidation is performed by an oxygen plasma treatment. Such treatments are also commonly applied to ITO electrodes fabricated by vapor phase deposition, before they are used for organic semiconductor solar cell preparation, because the plasma treatment of the electrodes improves the device performances.[28,29] Thus in respect to device fabrication, the plasma treatment applied here for NC oxidation, does not represent an extra effort. In the case of our NC films, the oxygen plasma treatment has several consequences, as is revealed in detail by transmission electron microscopy imaging of a self-assembled monolayer of indium NCs (Figure 4). (i) Most apparently, by oxidation a large portion of the indium NCs becomes hollow (Figure 4B), due to the nanoscale Kirkendall effect.[9] The formation of hollow NCs by oxidation has been observed before, for example, for cobalt or iron NCs as starting materials,[9,30] and it results from a difference of diffusion rates between oxygen and the metal atoms followed by a condensation of supersaturated vacancies. (ii) The oxidation converts the indium NCs into In_2O_3, as is evidenced by the selected area electron diffraction patterns in Figure 4C,D. (iii) After oxidation,

the gaps in between the NCs are reduced considerably, indicating the removal of the organic ligand shell as well as an increase of the average NC size (Figure 4B, Supporting Information, Figure S9). The removal of the organic ligands is confirmed also by EDX spectra obtained from the deposited NC films (Figure S10), showing the disappearance of the C-peaks due to oxidation. The increase in diameter is partly caused by the increase of the unit cell volume (Figure S11) and partly by the formation of the cavities in the NC centers. While the increase in unit cell volume would cause a 6% increase in diameter, we observe an overall increase of NC diameters up to 22% (Figure S9). It is noted, that before oxidation the gaps between the NCs are very uniform with a size of 1.2 nm, while after oxidation the average NC distance is decreased to 0.4 nm, with a variety between zero and about twice the mean value before oxidation. Before oxidation the homogeneous gap distance is given by the organic ligand shell, while after oxidation the gaps result predominantly from the observed increase of NC size dispersion. (iv) The oxidation leads to a recrystallization of the NCs, starting from the surface and proceeding toward the center of the NCs. While the indium NCs exhibit predominantly a polycrystalline nature (Figure 4E), resulting from the fast cooling from liquid phase during the synthesis, after the plasma treatment each In_2O_3 NC is single crystalline (Figure 4F). Interestingly, short plasma treatments result in intermediate structures exhibiting an In/In_2O_3-core/hollow shell structure, with a common orientation of the In (sub-) lattices (Figure S11), irrespective of the 4.8% mismatch between their In (sub)lattice plane distances. The recrystallization might be thermally assisted since during plasma treatment the temperature inside the plasma chamber reaches values around 110 °C. (v) The oxidation of $In_{1-x}Sn_x$ NCs by plasma treatments gives analogous results as those obtained for the pure indium NCs. The oxidation in the plasma chamber does not change the initial Sn content (Figure S10), thus by controlling x of the $In_{1-x}Sn_x$ NCs allows the control of x in the final ITO NCs. Furthermore, the spherical shape of the NCs is maintained by the plasma treatment (Figure S9) and the size dispersion after oxidation is still below 5% for NC sizes between 10 and 23 nm ($x = 0-10$ atomic %).

Most importantly, the plasma oxidation changes the color, the transmittance, and the electrical conductivity of the NC assemblies. While for a thin film of $In_{1-x}Sn_x$ NCs, prepared by spin-casting the NCs on a glass substrate, the transmittance varies dependent on wavelength between 50% and 80% (Figure 5A), after the oxidation the transmittance is increased to values higher than 80−90%. The increase in transmittance is also associated with a color change from brown to almost totally transparent, as shown in Figure 5B,C for dried droplets of $In_{1-x}Sn_x$ NCs before and after oxidation. To obtain a first indication of the conductivity
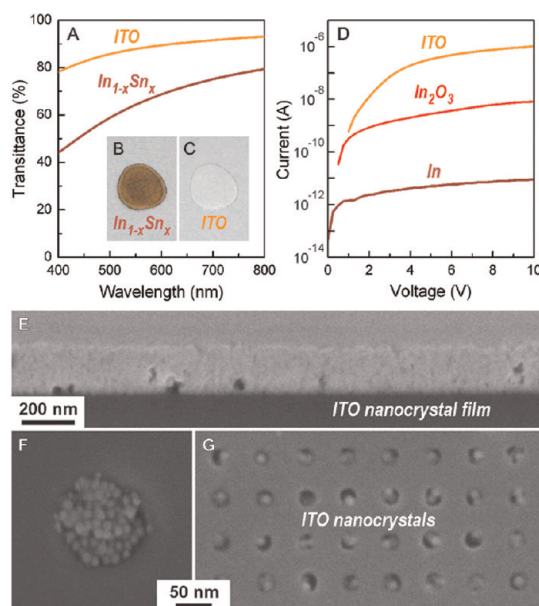

Figure 5. (A) Transmittance of a spin-casted $In_{1-x}Sn_x$ NC film before and after oxidation in oxygen plasma. (B,C) Photos of $In_{1-x}Sn_x$ NC droplets on a glass substrate, before and after oxidation. (D) $I-V$ characteristics, measured for indium NCs dropped on interdigital gold electrodes before and after oxidation (In_2O_3) and for $In_{1-x}Sn_x$ NCs after oxidation (ITO). (E) Cross-sectional SEM image showing a homogeneous ITO NC film with an average thickness of 200 nm, used for conductivity measurements. (F) SEM image of a ITO NC nanoelectrode, prepared in 100 nm pits on silicon substrate; (G) 25 nm pits occupied by single ITO NCs.

change upon annealing, droplets of the colloid were deposited on interdigital electrode structures, allowing $I-V$ characterization even for highly resistive samples. On these electrodes the pure indium NC films biased by a few volts across an electrode gap of 20 μm provide currents in the pA range (Figure 5D). Applying the plasma treatment to the indium NCs and thus removing the ligand shell and converting the indium to In_2O_3 increases the current by 3 orders of magnitude up to the nA region. If the same treatment is applied to $In_{1-x}Sn_x$ NCs with $x = 10$%, currents increase by up to 5 orders of magnitude compared to that before oxidation.

To study the conductivity of ITO films formed from the NCs, layers of uniform thickness were prepared by multiple spin-casting of $In_{1-x}Sn_x$ NCs on top of each other. After each spin-casting step, the NCs were cross-linked by a fast treatment with mercaptoacetic acid.[31] After oxidation by the plasma treatment, platinum contacts were sputtered on top of the film, enabling accurate conductivity measurements by the four-probe method. To date, in ITO NC films high conductivity was obtained only after mechanically pressing the NCs to pellets or after heat treatments.[4−7] For our samples heating in air to 420 °C for 40 min gives the lowest specific resistivity. Taking into account the film thickness, measured by cross-sectional SEM imaging to

be close to 200 nm (Figure 5E), results in a specific resistance of 2.6×10^{-2} $\Omega \cdot cm$, corresponding to a conductivity of 38 S·cm^{-1}. This conductivity is considerably smaller than the standard values obtained in vapor-deposited ITO films. It is mainly limited by a certain number of cavities and cracks in the ITO NC film (Figure 5E) as well as by small gaps between neighboring ITO NCs (Figure 4B). In comparison to other ITO electrodes obtained from nanoparticle solutions, this value is, however, at least equal to the best, recently reported values.[4−6] Furthermore, the obtained conductivity is in the same range as those of conducting polymers, such as poly(3,4-ethylenedioxythiophene), PEDOT,[32] or as doped polyacetylene,[33] which have been used frequently as electrodes in high performance organic field effect transistors.[34−36] This makes the ITO films of potential interest for applications as transparent electrodes in all-nanoparticle solution processed opto-electronic devices.

Since the same process steps as for the ITO NC films are also applied to the nanopatterns of NC self-assemblies, fabricated by the damascene process, it can be expected that after oxidation and heat treatment these patterns exhibit the same favorable properties, transparency and electrical conductivity, as the tested thin films. While the heat treatment affects greatly the conductivity in the NC film, it does not change the nanocrystallinity of it. This is clearly seen in the nanopatterns prepared by the damascene process, exhibiting after the heat treatment still an ensemble of individual NCs (Figure 5E, Supporting Information, Figure S8 shows even the same NC arrangement in a 100 nm pit, before and after plasma oxidation). Thus the NC ensembles in the 100 nm pits could be applied as ITO nanostructured electrodes of future opto-electronic devices, which might be also integrated with silicon electronics. The oxidation applied to the In$_{1−x}$Sn$_x$ NCs deposited by the damascene process into 25 nm pits results in single ITO NCs (Figure 5F),

which are probably hard to be contacted and used as nanoelectrodes. Nevertheless, they are of interest, especially due to their plasmon resonances observed in the near-infrared,[37,38] which can be applied for plasmon enhanced optical effects, as are commonly observed with gold nanoparticles in the visible spectral region. In this context the deposition of individual NCs is of interest because it makes each NC addressable by techniques such as confocal microscopy.

CONCLUSIONS

A fabrication procedure of nanopatterned ITO electrodes is introduced, representing a cost and material effective alternative to the standard processes based on vapor phase deposition, followed by top down structuring. The procedure includes three steps: (i) the synthesis of monodisperse In$_{1−x}$Sn$_x$ colloidal NCs, (ii) the preparation of self-assembled thin films and nanosized structures from these NCs, and (iii) complete oxidation of the NC assemblies. The 8 to 19 nm large In$_{1−x}$Sn$_x$ NCs, synthesized via a nucleation controlled hot-injection of silylamide salts into amine, exhibit almost perfect spherical shapes and extremely narrow size distributions, down to 2.2%. This unique monodispersity results in a high tendency to form ordered superstructures with high filling factors, observed in 3D microcrystallites as well as in thin films, obtained simply by drop casting. Oxidation of the NCs in oxygen plasma converts the In$_{1−x}$Sn$_x$ NCs into optically transparent and electrically conductive ITO. The conductivity is at least as good as those obtained from ITO nanoparticle inks, the monodispersity of the used In$_{1−x}$Sn$_x$ NCs, however, enables also the fabrication of nanosized electrodes with lateral dimensions as small as 25 nm. Such nanopatterned ITO electrodes on silicon substrates might be used in the future for integration of solution processed opto-electronic nanodevices onto standard silicon-electronics.

EXPERIMENTAL SECTION

Materials. Indium(III) chloride (99.99%), tin(II) bis[bis-(trimethylsilyl)amide] (Sn[N(SiMe$_3$)$_2$]$_2$, purum grade), lithium bis(trimethylsilyl)amide (Li[N(SiMe$_3$)$_2$], 97%), oleic acid (OA, 90%), lithium triethylborohydride (Li[Et$_3$BH], 1.0 M solution in tetrahydrofuran), mercaptoacetic acid (≥98%), toluene (anh. 99.9%), tetrachloroethylene (≥99.9%), diethyl ether (anh. ≥99.7%), pentane (anh. ≥99%), butanol (anh. 99.8%), ethanol (99.8%), indium wire (99.999%), and tin shots (99.999%) were purchased from Sigma-Aldrich; hexadecylamine (HDA, techn., ≥90%, contains tetradecylamine ~3%, and octadecylamine ~3%) from Fluka. All were used without further purification.

Synthesis of Indium(III) Tris[bis(trimethylsilyl)amide]. Since the precursor for the synthesis of the indium NCs, In[N(SiMe$_3$)$_2$]$_3$, is not commercially available, it has to be synthesized prior to the NC growth, according to Bürger et al.[39] All steps were performed under oxygen- and water-free atmosphere. InCl$_3$ (6.6 mmol) was dissolved in diethylether (80 mL) at 60 °C, forming a colorless solution. In another bottle, a solution of Li[N(SiMe$_3$)$_2$] (20 mmol)

in diethylether (40 mL) was prepared, and then added dropwise to the InCl$_3$ solution kept at 60 °C under stirring. White precipitates of LiCl are formed continuously during the metathesis reaction. After 24 h of continuous stirring, the reaction was stopped and cooled to room temperature and the precipitates were filtered from solution by a Teflon filter (pore size 450 nm). The filtered pale-yellow solution was placed under vacuum to remove the solvent. As a result, white powder was obtained which was dissolved in anhydrous pentane (15 mL), filtered, and placed under vacuum again. The In[N(SiMe$_3$)$_2$]$_3$ crystalline powder has a color between white and pale yellow, and it was stored in a glovebox for further use.

Synthesis of Indium Nanocrystals. In a typical experiment HDA (20 g) was loaded in a three neck flask and heated to 100 °C for 1 h for purification. Subsequently, the temperature of the liquid HDA was increased to 200 °C, where it was kept in argon atmosphere for another 30 min. In the meantime, two injection solutions were prepared inside a glovebox and loaded into syringes. Solution 1: In[N(SiMe$_3$)$_2$]$_3$ (0.26 g) and Li[N(SiMe$_3$)$_2$] (0.728 g) dissolved in

anhydrous toluene (8 mL). The In[N(SiMe$_3$)$_2$]$_3$ to Li[N(SiMe$_3$)$_2$] molar ratio was kept as 1:10 for all experiments. Solution 2: 1.0 M THF solution of Li[Et$_3$BH] (100 μL). Solution 1 was swiftly added to the 200 °C hot HDA, which resulted in a bright-yellow solution. Approximately 1 min later, solution 2 was injected into the reaction mixture. The color of the solution changed to deep brown, indicating the indium NC formation. During the time between the injection of solution 1 and solution 2, the temperature of the reaction mixture reached a stable value of 155 °C, being the boiling point of the HDA/toluene reaction mixture.

After a certain time of NC growth, the solution was cooled with a water bath. The indium NCs were separated by subsequent additions of toluene (20 mL) and ethanol (40 mL) under ambient condition. This was followed by centrifugation at 6000 rpm for 5 min, after which the supernatant was discarded. Tetrachloroethylene (10 mL) was added to the precipitates along with oleic acid (200 μL). All washing steps were repeated three times, and they resulted in colloids of indium NCs, which are stable in any common nonpolar solvent. A synthesis yield up to 40−50% was achieved, and NC concentrations up to 50 mg/mL were obtained.

Synthesis of Indium Tin Alloyed Nanocrystals. In$_{1−x}$Sn$_x$ NCs were obtained similarly to the above given recipe for indium NCs. Here, solution (1) additionally contained a certain amount of Sn[N(SiMe$_3$)$_2$]$_2$. The amount of Sn[N(SiMe$_3$)$_2$]$_2$ determines the composition of the indium tin NCs: $x(\%) = 0.21 \cdot V$, where x is the tin concentration in the NCs and V is the amount of Sn[N(SiMe$_3$)$_2$]$_2$ in microliters.

Preparation of 2D and 3D Self-Assemblies of Nanocrystals. Self-assembled monolayers of NCs were prepared by drop casting of NCs solved in tetrachloroethylene on a polished and HF-treated silicon substrate. The concentration of the solution was in the range of 0.3−1 mg/mL. Slight tilting of the samples (like 10°) improved the self-assembly properties.

The growth of 3D supercrystals was performed *via* slow destabilization of NC solutions.[24] For that purpose, the solution of NCs was separated by two buffer layers from a nonsolvent. The NC solution in tetrachloroethylene (1 mL, 3−5 mg/mL) was placed in test tubes with an inner diameter of 8 mm and a length of 75 mm. Two buffer layers of toluene and butanol (0.5 mL each) were subsequently added and then 1.5 mL of ethanol was introduced. All steps were handled slowly, and the test tubes were slightly tilted. The tubes were closed in N$_2$-atmosphere and placed in darkness for 2 weeks. Afterward, the supercrystals were collected from the bottom and the side walls of the tubes. Colloidal microcrystals were isolated by decantation and sedimentation in anhydrous ethanol repeated three times.

Preparation of Prepatterned Silicon Substrates. The pit-shaped prepatterned silicon substrates were prepared by electron beam lithography and dry etching. To achieve the high resolution patterns required to obtain 25 nm small pits, a VISTEC VB6 (vector beam) electron beam writer has been used with an accelerating voltage of 100 keV using polymethylmethacrylate (PMMA) as resist material. The accurate control of the depth of 25 nm is obtained by reactive ion etching (RIE) with an ICP 380 source operating at −80 °C with a RF power of 50 W in an Oxford Plasmalab System 100. The substrates with pit diameter of 100 nm were prepared on a LEO Supra 35 system with a Raith Elphy electron beam writing unit working at 30 keV, combined with the RIE procedures. In this case the average pit depth is about 40 nm. For both types of substrates, SF$_6$/O$_2$ has been used as working gas.

Preparation of Nanopatterned Electrodes with Damascene Processing. NCs solved in tetrachloroethylene were adsorbed onto the prepatterned silicon substrate by drop-casting. The concentration of the solution was in the range between 0.3 and 1 mg/mL. After evaporation, the prepatterned substrates were covered with closely packed NC films. After deposition the substrates were mechanically polished for 2 min with a homemade processing plate covered with a commercial polishing cloth (Mastertex PSA, BUEHLER GmbH). This procedure removed the excessive NCs from the flat surface parts of the substrates, whereas the NCs in the pits remained.[8]

Oxidation of Indium and Indium Tin Nanocrystals. The NC thin films and nanopatterned electrodes were oxidized with an oxygen plasma reactor (300-MULTISTEP, Technics Plasma Gmbh, 100−300 W). The oxygen flow was 100 mL/min, and the radio frequency power was 300 W to obtain a fast oxidation. The time of plasma treatment was typically 30 min.

Nanocrystal Characterization. SEM images were recorded a JEOL JSM-6400 SEM microscope. This microscope is also equipped with an X-ray detector used for EDX analysis. Characteristic X-ray lines can be detected in a range of 0−20 keV. A JEOL 2011 FasTEM microscope was used for (high resolution) TEM imaging as well as for measuring selected area electron diffraction patterns. The size distributions are given as standard deviations from mean values, measured from the TEM images for at least 100 NCs in all cases. Wide angle X-ray spectra were measured by a custom-built rotating anode X-ray diffractometer, by using the Cu Kα line (1.5419 Å) and a Vantec PSD detector. The unit cell parameters for the In$_{1−x}$Sn$_x$ NCs were deduced by fitting the spectra with *fityk* software.[40] The intensity ratio between Kα_1 and Kα_2, determined experimentally to be 1:0.47, was used for *fityk* refinements.

Conflict of Interest: The authors declare no competing financial interest.

Supporting Information Available: Supporting Figures S1−S11 with descriptions. This material is available free of charge *via* the Internet at http://pubs.acs.org.

REFERENCES AND NOTES

1. Tessler, N.; Medvedev, V.; Kazes, M.; Kan, S.; Banin, U. Efficient Near-Infrared Polymer Nanocrystal Light-Emitting Diodes. *Science* **2002**, *295*, 1506–1508.
2. Caruge, J. M.; Halpert, J. E.; Wood, V.; Bulovic, V.; Bawendi, M. G. Colloidal Quantum-Dot Light-Emitting Diodes with Metal-Oxide Charge Transport Layers. *Nat. Photon.* **2008**, *2*, 247–250.
3. McDonald, S. A.; Konstantatos, G.; Zhang, S.; Cyr, P. W.; Klem, E. J. D.; Levina, L.; Sargent, E. H. Solution-Processed PbS Quantum Dot Infrared Photodetectors and Photovoltaics. *Nat. Mater.* **2005**, *4*, 138–142.
4. Ba, J.; Rohlfing, D. F.; Feldhoff, A.; Brezesinski, T.; Djerdj, I.; Wark, M.; Niederberger, M. Nonaqueous Synthesis of Uniform Indium Tin Oxide Nanocrystals and Their Electrical Conductivity in Dependence of the Tin Oxide Concentration. *Chem. Mater.* **2006**, *18*, 2848–2854.
5. Bühler, G.; Thölmann, D.; Feldmann, C. One-Pot Synthesis of Highly Conductive Indium Tin Oxide Nanocrystals. *Adv. Mater.* **2007**, *19*, 2224–2227.
6. Gilstrap, R. A.; Capozzi, C. J.; Carson, C. G.; Gerhardt, R. A.; Summers, C. J. Synthesis of a Nonagglomerated Indium Tin Oxide Nanoparticle Dispersion. *Adv. Mater.* **2008**, *20*, 4163–4166.
7. Sasaki, T.; Endo, Y.; Nakaya, M.; Kanie, K.; Nagatomi, A.; Tanoue, K.; Nakamura, R.; Muramatsu, A. One-Step Solvothermal Synthesis of Cubic-Shaped ITO Nanoparticles Precisely Controlled in Size and Shape and Their Electrical Resistivity. *J. Mater. Chem.* **2010**, *20*, 8153–8157.
8. Chen, G.; Bodnarchuk, M. I.; Kovalenko, M. V.; Springholz, G.; Heiss, W.; Jantsch, W.; Platzgummer, E.; Loeschner, H.; Schotter, J. Damascene Process for Controlled Positioning of Magnetic Colloidal Nanocrystals. *Adv. Mater.* **2010**, *22*, 1364–1368.
9. Yin, Y.; Rioux, R. M.; Erdonmez, C. K.; Hughes, S.; Somorjai, G. A.; Alivisatos, A. P. Formation of Hollow Nanocrystals

through the Nanoscale Kirkendall Effect. *Science* **2004**, *304*, 711–714.

10. Soulantica, K.; Maisonnat, A.; Senocq, F.; Fromen, M.-C.; Casanove, M.-J.; Chaudret, B. Selective Synthesis of Novel In and In$_3$Sn Nanowires by an Organometallic Route at Room Temperature. *Angew. Chem.* **2001**, *113*, 3071–3074.

11. Zhao, Y.; Zhang, Z.; Dang, H. Synthesis of In–Sn Alloy Nanoparticles by a Solution Dispersion Method. *J. Mater. Chem.* **2004**, *14*, 299–302.

12. Soulantica, K.; Maisonnat, A.; Fromen, M.-C.; Casanove, M.-J.; Lecante, P.; Chaudret, B. Synthesis and Self-Assembly of Monodisperse Indium Nanoparticles Prepared from the Organometallic Precursor [In(η^5-C$_5$H$_5$)]. *Angew. Chem.* **2001**, *113*, 462–465.

13. Soulantica, K.; Erades, L.; Sauvan, M.; Senocq, F.; Maisonnat, A.; Chaudret, B. Synthesis of Indium and Indium Oxide Nanoparticles from Indium Cyclopentadienyl Precursor and Their Application for Gas Sensing. *Adv. Funct. Mater.* **2003**, *13*, 553–557.

14. Chou, N. H.; Ke, X.; Schiffer, P.; Schaak, R. E. Room-Temperature Chemical Synthesis of Shape-Controlled Indium Nanoparticles. *J. Am. Chem. Soc.* **2008**, *130*, 8140–8141.

15. Yu, H.; Gibbons, P. C.; Kelton, K. F.; Buhro, W. E. Heterogeneous Seeded Growth: A Potentially General Synthesis of Monodisperse Metallic Nanoparticles. *J. Am. Chem. Soc.* **2001**, *123*, 9198–9199.

16. Kind, C.; Feldmann, C. One-Pot Synthesis of In^0 Nanoparticles with Tuned Particle Size and High Oxidation Stability. *Chem. Mater.* **2011**, *23*, 4982–4987.

17. Brown, H. C.; Kim, S. C.; Krishnamurthy, S. Selective Reductions. 26. Lithium Triethylborohydride as an Exceptionally Powerful and Selective Reducing Agent in Organic Synthesis. Exploration of the Reactions with Selected Organic Compounds Containing Representative Functional Groups. *J. Org. Chem.* **1980**, *45*, 1–12.

18. Yarema, M.; Kovalenko, M. V.; Hesser, G.; Talapin, D. V.; Heiss, W. Highly Monodisperse Bismuth Nanoparticles and Their Three-Dimensional Superlattices. *J. Am. Chem. Soc.* **2010**, *132*, 15158–15159.

19. Koyama, Y.; Ukena, T.; Morikawa, K.; Nittono, O. Martensitic Transformations in Indium-(13-X) at% Lead-X at% Tin Pseudobinary Alloys. *J. Japan Inst. Met.* **1983**, *47*, 919–926.

20. Villars, P.; Girgis, K. Phase Diagrams Nb–In, Nb–Tl, Ta–In and Ta–Tl. *Z. Metallkd.* **1982**, *73*, 169–171.

21. Eckerlin, P.; Kandler, H. Structure Data of Elements and Intermetallic Phases. *Landolt-Börnstein* **1971**, *6*, 670.

22. Bodnarchuk, M. I.; Kovalenko, M. V.; Heiss, W.; Talapin, D. V. Energetic and Entropic Contributions to Self-Assembly of Binary Nanocrystal Superlattices: Temperature as the Structure-Directing Factor. *J. Am. Chem. Soc.* **2010**, *132*, 11967–11977.

23. Evers, W. H.; De Nijs, B.; Filion, L.; Castillo, S.; Dijkstra, M.; Vanmaekelbergh, D. Entropy-Driven Formation of Binary Semiconductor-Nanocrystal Superlattices. *Nano Lett.* **2010**, *10*, 4235–4241.

24. Rogach, A. L.; Talapin, D. V.; Shevchenko, E. V.; Kornowski, A.; Haase, M.; Weller, H. Organization of Matter on Different Size Scales: Monodisperse Nanocrystals and Their Superstructures. *Adv. Funct. Mater.* **2002**, *12*, 653–664.

25. Pichler, S.; Bodnarchuk, M. I.; Kovalenko, M. V.; Yarema, M.; Springholz, G.; Talapin, D. V.; Heiss, W. Evaluation of Ordering in Single-Component and Binary Nanocrystal Superlattices by Analysis of Their Autocorrelation Functions. *ACS Nano* **2011**, *5*, 1703–1712.

26. Shevchenko, E. V.; Talapin, D. V.; Kotov, N. A.; O'Brien, S.; Murray, C. B. Structural Diversity in Binary Nanoparticle Superlattices. *Nature* **2006**, *439*, 55–59.

27. Vanmaekelbergh, D. Self-Assembly of Colloidal Nanocrystals as Route to Novel Classes of Nanostructured Materials. *Nano Today* **2011**, *6*, 419–437.

28. Wu, C. C.; Wu, C. I.; Sturm, J. C.; Kahn, A. Surface Modification of Indium Tin Oxide by Plasma Treatment: An Effective Method to Improve the Efficiency, Brightness, and Reliability of Organic Light Emitting Devices. *Appl. Phys. Lett.* **1997**, *70*, 1348–1350.

29. Kim, J. S.; Granstrom, M.; Friend, R. H.; Johansson, N.; Salaneck, W. R.; Daik, R.; Feast, W. J.; Cacialli, F. Indium-Tin Oxide Treatments for Single- and Double-Layer Polymeric Light-Emitting Diodes: The Relation between the Anode Physical, Chemical, and Morphological Properties and the Device Performance. *J. Appl. Phys.* **1998**, *84*, 6859–6870.

30. Shevchenko, E. V.; Bodnarchuk, M. I.; Kovalenko, M. V.; Talapin, D. V.; Smith, R. K.; Aloni, S.; Heiss, W.; Alivisatos, A. P. Gold/Iron Oxide Core/Hollow-Shell Nanoparticles. *Adv. Mater.* **2008**, *20*, 4323–4329.

31. Pattantyus-Abraham, A. G.; Kramer, I. J.; Barkhouse, A. R.; Wang, X.; Konstantatos, G.; Debnath, R.; Levina, L.; Raabe, I.; Nazeeruddin, M. K.; Grätzel, M.; Sargent, E. H. Depleted-Heterojunction Colloidal Quantum Dot Solar Cells. *ACS Nano* **2010**, *4*, 3374–3380.

32. Groenendaal, L.; Jonas, F.; Freitag, D.; Pielartzik, H.; Reynolds, J. R. Poly(3,4-ethylenedioxythiophene) and Its Derivatives: Past, Present, and Future. *Adv. Mater.* **2000**, *12*, 481–494.

33. Chiang, C. K.; Fincher, C. R.; Park, Y. W.; Heeger, A. J.; Shirakawa, H.; Louis, E. J.; Gau, S. C.; MacDiarmid, A. G. Electrical Conductivity in Doped Polyacetylene. *Phys. Rev. Lett.* **1977**, *39*, 1098–1101.

34. Sirringhaus, H.; Kawase, T.; Friend, R. H.; Shimoda, T.; Inbasekaran, M.; Wu, W.; Woo, E. P. High-Resolution Inkjet Printing of All-Polymer Transistor Circuits. *Science* **2000**, *290*, 2123–2126.

35. Li, D.; Guo, L. J. Micron-Scale Organic Thin Film Transistors with Conducting Polymer Electrodes Patterned by Polymer Inking and Stamping. *Appl. Phys. Lett.* **2006**, *88*, 063513.

36. Hong, K.; Kim, S. H.; Yang, C.; An, T. K.; Cha, H.; Park, C.; Park, C. E. Photopatternable, Highly Conductive and Low Work Function Polymer Electrodes for High-Performance n-Type Bottom Contact Organic Transistors. *Org. Electron.* **2011**, *12*, 516–519.

37. Kanehara, M.; Koike, H.; Yoshinaga, T.; Teranishi, T. Indium Tin Oxide Nanoparticles with Compositionally Tunable Surface Plasmon Resonance Frequencies in the Near-IR Region. *J. Am. Chem. Soc.* **2009**, *131*, 17736–17737.

38. Garcia, G.; Buonsanti, R.; Runnerstrom, E. L.; Mendelsberg, R. J.; Llordes, A.; Anders, A.; Richardson, T. J.; Milliron, D. J. Dynamically Modulating the Surface Plasmon Resonance of Doped Semiconductor Nanocrystals. *Nano Lett.* **2011**, *11*, 4415–4420.

39. Bürger, H.; Cichon, J.; Goetze, U.; Wannagat, U.; Wismar, H. J. Beiträge zur Chemie der Silicium-Stickstoff-Verbindungen. Darstellung, Schwingungsspektren und Normalkoordinatenanalyse von Disilylamiden der 3 Gruppe: M[N(SiMe$_3$)$_2$]$_3$ mit M = Al, Ga und In (Contributions to the chemistry of silicon–nitrogen compounds. Representation, vibrational spectra, and normal coordinate analysis of the 3rd Disilylamiden Group M[N(SiMe$_3$)$_2$]$_3$ with M = Al, Ga, and In). *J. Organomet. Chem.* **1971**, *33*, 1–12.

40. Wojdyr, M. Fityk: a General-Purpose Peak Fitting Program. *J. Appl. Crystallogr.* **2010**, *43*, 1126–1128.